



RESEARCH ARTICLE

10.1029/2020JB020433

Key Points:

- We present a three-dimensional anisotropic P wave velocity model in northern Hikurangi from traveltime tomography using NZ3D OBS data
- We find evidence for fault-bound anisotropy that azimuthal anisotropy is larger in the vicinity of the splay faults and deformation front
- Anisotropy magnitude $>5\%$ may indicate preferentially oriented cracks and along-fault clay-rich layers contribute to upper plate anisotropy

Supporting Information:

- Supporting Information S1

Correspondence to:

R. Arai,
ryuta@jamstec.go.jp

Citation:

Arai, R., Kodaira, S., Henrys, S., Bangs, N., Obana, K., Fujie, G., et al. (2020). Three-dimensional P wave velocity structure of the northern Hikurangi margin from the NZ3D experiment: Evidence for fault-bound anisotropy. *Journal of Geophysical Research: Solid Earth*, 125, e2020JB020433. <https://doi.org/10.1029/2020JB020433>

Received 19 JUN 2020










Accepted 11 NOV 2020

Accepted article online 17 NOV 2020

©2020. The Authors.

This is an open access article under the terms of the Creative Commons Attribution License, which permits use, distribution and reproduction in any medium, provided the original work is properly cited.

Three-Dimensional P Wave Velocity Structure of the Northern Hikurangi Margin From the NZ3D Experiment: Evidence for Fault-Bound Anisotropy

Ryuta Arai¹ , Shuichi Kodaira¹ , Stuart Henrys² , Nathan Bangs³ , Koichiro Obana¹, Gou Fujie¹ , Seiichi Miura¹, Daniel Barker² , Dan Bassett², Rebecca Bell⁴, Kimihiro Mochizuki⁵ , Richard Kellett² , Valerie Stucker² , Bill Fry², and NZ3D Team

¹Research Institute for Marine Geodynamics, Japan Agency for Marine-Earth Science and Technology (JAMSTEC), Yokohama, Japan, ²GNS Science, Lower Hutt, New Zealand, ³Institute for Geophysics, University of Texas at Austin, Austin, TX, USA, ⁴Imperial College London, London, UK, ⁵Earthquake Research Institute, University of Tokyo, Tokyo, Japan

Abstract We present a high-resolution three-dimensional (3-D) anisotropic P wave velocity (V_p) model in the northern Hikurangi margin offshore Gisborne, New Zealand, constructed by tomographic inversion of over 430,000 first arrivals recorded by a dense grid of ocean bottom seismometers. Since the study area covers a region where shallow slow slip events (SSEs) occur repeatedly and the subduction of a seamount is proposed, it offers an ideal location to link our understanding of structural and hydrogeologic properties at megathrust faults to slip behavior. The V_p model reveals an ~ 30 -km-wide, low-velocity accretionary wedge at the toe of the overriding plate, where previous seismic reflection studies show a series of active thrust faults branching from the plate interface. We find some locations with significant V_p azimuthal anisotropy $>5\%$ near the branching faults and the deformation front. This finding suggests that the anisotropy is not ubiquitous and homogeneous within the overriding plate, but more localized in the vicinity of active thrust faults. The fast axes of V_p within the accretionary wedge are mostly oriented to the plate convergence direction, which is interpreted as preferentially oriented cracks in a compressional stress regime associated with plate subduction. We find that the magnitudes of anisotropy are roughly equivalent to values found at oceanic spreading centers, where the extensional stress regime is dominant and the crack density is expected to be higher than subduction zones. This consideration may indicate that additional effects such as fault foliation and clay mineral alignment also contribute to upper plate anisotropy along subduction margins.

Plain Language Summary We use man-made sound waves (controlled-source seismic data) to reveal in three dimensions the speed of sound within rocks and sediments that make up the northern Hikurangi margin off the east coast of North Island, New Zealand. We find that the sediments lying on top of subducting plate (accretionary wedge) have low velocities and host several branching faults. We also find that the speed of sound is faster when measured in the direction that the plates are colliding and slower when measured parallel to the faults (this phenomenon is called seismic anisotropy). This difference in speed suggests that the faults contain cracks that are aligned parallel to the direction of the plate subduction.

1. Introduction

The Hikurangi subduction margin, New Zealand (Figure 1), has not experienced any major ($M_w > 7.2$) subduction interface earthquakes since historical record keeping began ~ 160 years ago (Webb & Anderson, 1998). The overriding Australian plate, by contrast, has produced 10 large ($M_w > 7.0$), damaging earthquakes over the same period (Webb & Anderson, 1998). Paleoseismic interpretations reveal that up to 10 subduction earthquakes may have occurred in the past 7,000 years, with the strongest evidence for a full Hikurangi margin rupture occurring 870–815 years before present, potentially with $M_w > 9.0$ (Clark et al., 2019). However, a diverse array of aseismic creep and slow slip event (SSE) behavior has also been documented along the Hikurangi subduction interface (Wallace, 2020). In the northern part of the margin, offshore Gisborne, frequent (18- to 24-months recurrence intervals), small (moment releases of $M_w = 6.3$ –

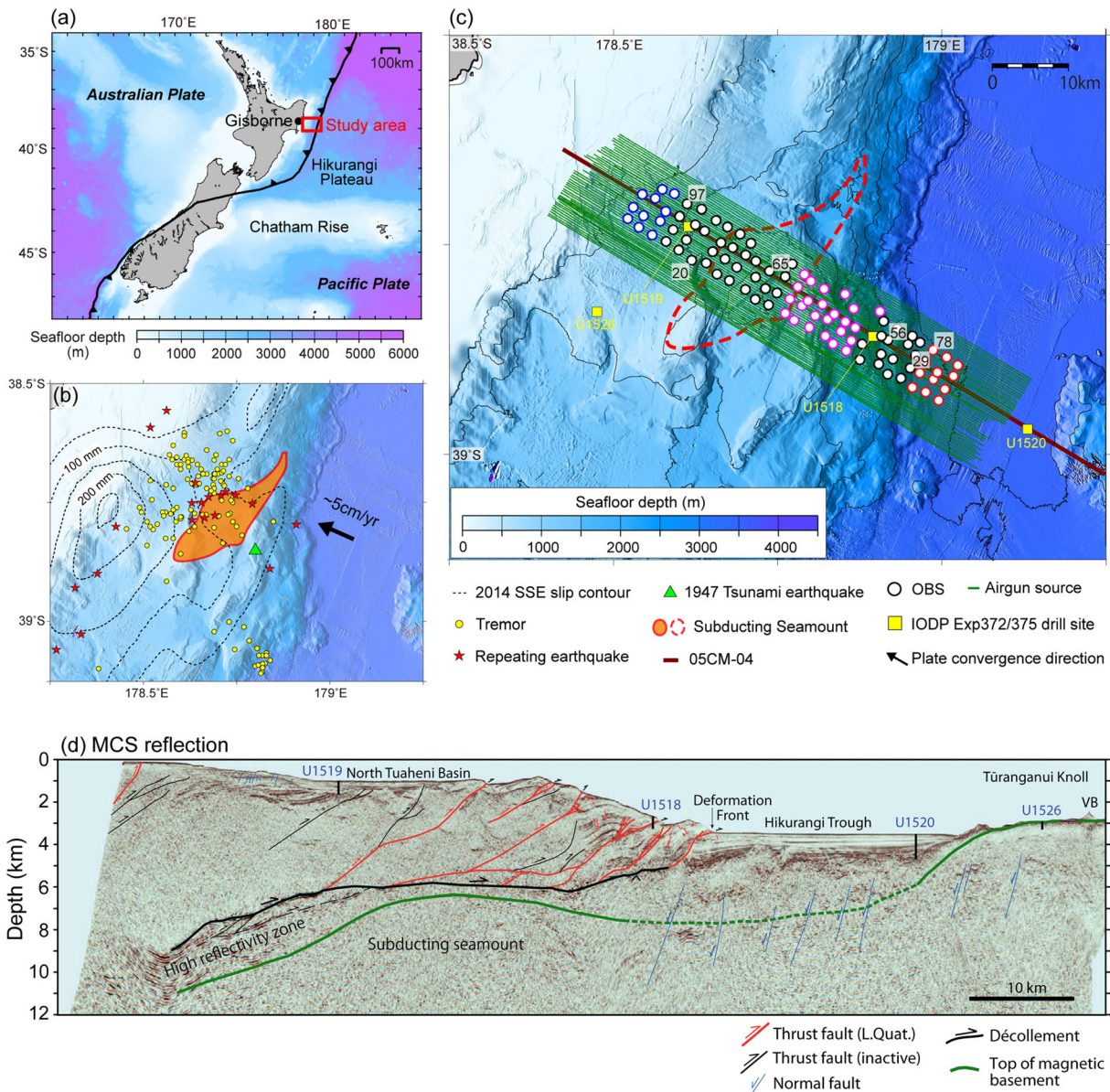


Figure 1. (a) Regional tectonic map of New Zealand. The black solid line is the plate boundary between the Pacific plate and Australian plate from Bird (2003). The black box indicates the location of 1b and 1c. (b) Seismic activity in the study area. Black dashed contours indicate the slip amount (in millimeter) of the SSE in 2014 (Wallace et al., 2016). Yellow dots, red stars, and a green triangle are the locations of tremor (Todd et al., 2018), burst-type repeating earthquakes (Shaddox & Schwartz, 2019) and the tsunami earthquake in 1947 (Doser & Webb, 2003), respectively. The location of inferred subducting seamount (orange shade delineated by the red line) is from Barker et al. (2018). The black arrow shows the convergence direction of the Pacific Plate relative to the North Island at the Hikurangi Trough (Wallace et al., 2004). (c) Layout of the NZ3D OBS experiment. White circles indicate the locations of OBSs. Numbered locations correspond with OBSs indicated in Figure 2. White circles with a colored circumference (red, purple, and blue) correspond to three groups on the difference geological units (incoming plate, accretionary wedge, and forearc basin) that are used to show the spatial variation in traveltime residual in Figure 6. Dark green lines are locations of air gun sources. Yellow squares are the locations of four IODP Exp372/375 drill sites (Wallace et al., 2019). Brown line shows the multichannel seismic reflection profile of 05CM-04 (Bell et al., 2010; Barker et al., 2018; Gray et al., 2019; Figure 1d). The red dashed line marks the outline of location of the inferred subducting seamount (Barker et al., 2018). (d) The 05CM-04 seismic reflection image (Barker et al., 2018; Wallace et al., 2019).

6.8) SSEs occur at <10- to 15-km depths (Wallace & Beavan, 2010; Wallace et al., 2016). This area is also known to have hosted two large tsunami earthquakes in 1947 (Bell et al., 2014; Doser & Webb, 2003). Despite the importance for assessing seismogenic and tsunami potentials, the physical properties of the shallow megathrust faults and splay faults and their three-dimensional variation are poorly documented and underlying mechanisms controlling the spatial variability in megathrust slip behavior remain largely unknown.

In 2017–2018, an intensive seismic imaging project NZ3D was carried out in the northern Hikurangi margin (Figure 1c). This project consisted of three components; a 3-D multichannel seismic (MCS) reflection profiling (MGL1801 participants, 2018), a 3-D high-resolution ocean bottom seismograph (OBS) experiment (Kellett et al., 2018), and a 3-D onshore seismic observation (Bell et al., 2019). The NZ3D aims to comprehensively understand the 3-D structural, stratigraphic, and hydrogeologic properties along the subduction megathrust faults where a range of slip behavior is observed. The offshore NZ3D survey area overlaps the previously acquired 2-D MCS reflection profile of 05CM-04 (Barker et al., 2018; Bell et al., 2010; Figure 1), ongoing passive seismic and geodetic monitoring studies (Shaddox & Schwartz, 2019; Todd et al., 2018; Wallace et al., 2016) and International Ocean Discovery Program (IODP) Drilling Expeditions 372 and 375 (Pecher et al., 2019; Wallace et al., 2019). The offshore Gisborne area thus provides one of the most comprehensive geophysical/geological datasets across a subduction zone and enables understanding of properties and behaviors of shallow subduction faults. In this paper, we present a detailed P wave velocity (V_p) model derived from the NZ3D OBS experiment. We determine compressional wave azimuthal anisotropy, which contributes to understanding crustal stress heterogeneity at lateral scales of a few kilometers. Our results are compared with logging data, borehole breakouts, shear wave splitting anisotropy, and mapped faults. This comparison is important since this may constrain possible variations in structure, stress, and their interpretation with depth at subduction zones.

2. Geological Setting

Along the ~500-km-long Hikurangi subduction zone, the oceanic Hikurangi Plateau, a large igneous province of Cretaceous age, is subducting beneath the North Island of New Zealand (e.g., Wood & Davy, 1994). The Hikurangi Plateau includes numerous seamounts and other volcanic features and is composed of basaltic basement thickly overlain by sedimentary layers of Mesozoic to Cenozoic ages (Barnes et al., 2020; Davy et al., 2008). Recent seismic surveys confirmed that the crust is over 10 km thick, and its thickness gradually increases from north to south in accordance with the latitudinal variation in seafloor depth (Kodaira et al., 2018; Mochizuki et al., 2019). In the northern part of the plateau where the seafloor is deeper (>3,000 m), more seamounts emerge on the seafloor, but the southern part of the plateau also hosts a number of basement highs that are buried by thick sediments (Kodaira et al., 2018; Mochizuki et al., 2019). Correspondingly, the thickness of the trench-fill sediments varies significantly along the trench from approximately 1 km in the north to >5 km in the south, which drives a progressive increase in the magnitude and extent of frontal accretion along the margin (Barnes et al., 2010).

The subduction of the Hikurangi Plateau at the Hikurangi margin is thought to have been initiated in the late Oligocene to early Miocene (Ballance, 1976; Lamb & Bibby, 1989; Rait et al., 1991). The current convergence rate progressively decreases from 58 mm/year in the north to 19 mm/year in the south (Wallace et al., 2004). The direction of the convergence is almost perpendicular to the trench in the north, but it is highly oblique to the trench strike in the south. The present interplate coupling rate also changes latitudinally with a sudden transition at ~40°S: To the north, the margin is characterized by low interplate coupling and shallow (<10 km) SSEs. To the south, a zone of strong coupling extends to depths of >40 km and is flanked downdip by regions hosting SSEs (Wallace, 2020). Seismic reflection studies recognized several subducting seamounts and high reflectivity zones in the source regions of the SSEs (Barker et al., 2009; Bell et al., 2010). The reflective zones are typically interpreted to be fluid-rich sediments entrained deep into the subduction zone by the subducting seamounts.

In the northern margin where the plate interface experiences SSEs at shallow depth, the forearc is characterized by a narrow-imbricated structure consisting of late Cenozoic accretionary prism at the toe of the overriding plate and landward Cretaceous to Paleogene rocks, both of which are variably covered by Miocene to recent sedimentary units (Barnes et al., 2010). The study area of our 3-D seismic experiment covers the Tuaheni ridge and the northern Tuaheni landslide complex on the upper continental slope. Within the accretionary prism, active landward-dipping thrust faults that splay off the plate interface are recognized (Bell et al., 2010; Barker et al., 2018; Figure 1d). Multichannel seismic (MCS) reflection and seafloor magnetic studies by Bell et al. (2010) and Barker et al. (2018) suggest that a large (30 × 10 km) seamount is subducting in this region and shallow tectonic tremors detected by Todd et al. (2018) are mostly located just

above and landward of the suspected seamount (Figure 1c). Using the same reflection data as Barker et al. (2018), Gray et al. (2019) derived a fine-scale velocity structure of the uppermost 1.5–2 km below the seafloor by applying a full-waveform inversion (FWI) technique and revealed sudden velocity changes within the frontal accretionary wedge indicating low-velocity zones along the splay faults, which may be related to fluid flow.

3. Seismic Anisotropy in the Crust of the Northern Hikurangi Margin

Stress field parameters can be measured using borehole breakouts, focal mechanisms of local earthquakes, shear wave splitting, and compressional wave azimuthal anisotropy. In the crust, anisotropy is mainly caused by either preexisting structural features, such as fault zones, or by the preferential closure of fluid filled fractures in response to the direction of horizontal compressive stress (Crampin, 1981). Differential horizontal stresses preferentially open the cracks that are oriented parallel to the maximum horizontal compressive stress (SH_{max}). Consequently, the magnitude of crack-controlled seismic anisotropy can be directly related to the magnitude of SH_{max} (e.g., Zatsepin & Crampin, 1997). It is also known that seismologically measurable anisotropy can be caused by the orientation of minerals in the rocks even in the absence of cracks. For example, Okaya et al. (1995) used rock samples from the Alpine Fault Zone in New Zealand to show that Haast schists and Torlesse greywackes exhibit several percent of anisotropy in V_p even in the plane of the foliation. Sedimentary rocks that are enriched in clay minerals and form a fine layering are another major source of seismic anisotropy at shallow depths (Wang, 2002).

The northern Hikurangi margin also provides an opportunity to examine the present-day variation in stress state in the upper and downgoing plates, knowledge of which is critical for understanding the storing and release of seismic energy (Townend et al., 2012; Zoback, 1992). Regional shear wave splitting analyses along the northern Hikurangi margin using local earthquakes show mainly NE-SW trench-parallel fast azimuths on the North Island (Audoine et al., 2004; Townend et al., 2012; Unglert, 2011). The NE-SW orientation of SH_{max} is also observed in the subducting plate beneath the North Island by Warren-Smith et al. (2019), using earthquake focal mechanisms, which is consistent with a normal faulting stress regime in the slab. By contrast, a comprehensive catalogue of anisotropy measurements based on passive seismic data along the margin (Illsley-Kemp et al., 2019), sampling the upper plate forearc, observe predominantly plate-motion parallel (E-W) fast orientations in the northern Hikurangi margin. Eberhart-Phillips and Reyners (2009) found that the Hikurangi margin forearc is characterized by heterogeneous anisotropy (both in magnitude and azimuth) using earthquake arrival time data. Shear wave splitting for event-station pairs on HOBITSS ocean bottom seismometers and onshore GeoNet seismic stations yields E-W fast azimuths in the accretionary wedge close to the trench and variable directions further landward, which may be explained by fracture and fault patterns created by subducting seamounts (Zal et al., 2020). Borehole breakouts at drill sites support that SH_{max} at shallow depths in the accretionary wedge is orthogonal to the deformation front (Wallace et al., 2019).

Shear wave splitting suffers poor spatial resolution in the depth direction since splitting properties are cumulative along the path for delay time. Shear waves may be re-split if they encounter a later and differing anisotropic layer, then a shallow secondary polarization instead of a deeper primary may be measured. Although a 3-D seismic refraction survey typically can sample only upper several kilometers crust, this method can overcome the issue of depth resolution by quantifying the variation in V_p as a function of the azimuth and depth of seismic raypaths throughout the 3-D volume. This approach can provide an accurate estimate of compressional wave azimuthal anisotropy at shallow depths (e.g., Dunn, 2015).

4. Seismic Data Acquisition and Description

The NZ3D OBS experiment acquired 3-D seismic refraction/wide-angle reflection data with multiazimuth ray coverage using the largest number of OBSs and densest air gun shooting in subduction zones to date. The seismic data were collected via a series of three marine expeditions. In December 2017, 100 OBSs of JAMSTEC were deployed by R/V *Tangaroa* with an average spacing of 2 km on four parallel lines across the Hikurangi Trough (Figure 1c). Each OBS contained hydrophone and three-component geophone sensors with natural frequency of 4.5 Hz. The sampling rate for recording was 200 Hz. In January–February 2018, the 3-D seismic reflection experiment was conducted by the U.S. R/V *Marcus G. Langseth* along 58

seismic lines with an average spacing of 300 m in the same area of the OBS network (MGL1801 participants, 2018). For this survey, over 140,000 air gun signals were triggered every 25 m in flip-flop mode and covered a 60-km × 14-km area extending from the northern Tuaheni landslide complex and the easterly forearc slope to the subduction trench (Figure 1c). The *Langseth* 36-element air gun array system was used as the seismic source. The air volume of each shot was 3,300 cubic inches and the towing depth was 7 m. Ninety-seven OBSs were successfully recovered by R/V *Tangaroa* in March–April 2018 (Kellett et al., 2018), all of which recorded the air gun signals generated from the *Langseth*.

After the recovery of the OBSs, the seafloor position of OBSs were determined using traveltimes of direct water waves. For locating OBSs, we used the method of Oshida et al. (2008) that comprises two steps of analysis. In the first step, a global search was performed at a grid interval of 0.0001° to find the node on the seafloor that best explains the observed arrival times of water waves. In the second step, the location determined by the first step was used as an initial point and a nonlinear inversion was carried out to improve the location estimation. The average 1σ location uncertainty calculated from traveltimes misfits are ~3 m. We then picked first arrivals manually. For picking, we used either hydrophone or vertical component data—whichever showed better data quality—and applied 3- to 12-Hz band-pass filter to improve the signal to noise ratio. The dense air gun shooting with 25-m interval designed for the 3-D reflection survey was not optimal for the OBS refraction study. Water waves from previous shots have high amplitude and overlap primary refraction phases from the next shot at horizontal distances between shot and receiver of ~25 and ~45 km, making it difficult to pick first arrivals at these offsets (Figure 2). Otherwise, the OBS data are of good quality and *P* wave first arrivals can be traced up to 20- to 50-km distance for most OBSs. Since the air gun shooting was much denser than typical refraction studies and produced significantly redundancy in the data, we picked first arrivals from every fifth shot line for all stations. To improve the ray coverage at deeper parts, we additionally picked other shot lines for some stations that have a good signal to noise ratio and clearly recorded long-offset first arrivals (Figures 2 and S1 in the supporting information). We assigned picking uncertainty of 0.030 s to traces in the offset range of 0–15 km. This value of uncertainty was chosen by examining the wavelength of first arrivals observed in the offset range. Thereafter, we increased the uncertainty to 0.040 s between an offset of 15–20 km because many OBS records show a significant amplitude reduction in this offset range. The uncertainty was further increased to 0.050 s at 20–30 km offset because the apparent velocity of first arrivals increases to ~6.0 km/s at this offset and the waveforms become more enriched in lower frequency compared to near-offset traces. Finally, the largest uncertainty of 0.060 s was assigned to traces >30 km offset where the first arrivals are possible to pick but contaminated by previous shot noise. For the tomography analysis, we used over 430,000 first arrivals.

In the seismic record sections, *P* waves with offset of <10 km arrive with apparent velocities less than 4.0 km/s, which indicates that the survey area is entirely covered by thick low-velocity sediments (Figure 2). OBSs on the landward side of the trench show a significant reduction in amplitude of refraction phases at 10- to 20-km distances. This feature is commonly observed at the forearc region of subduction zones and may suggest that there are shadow zones due to velocity reversals and/or highly attenuative zones caused by complex forearc structure. At farther offsets, first arrivals are refractions with apparent velocities of ~6.0 km/s for all the OBSs.

5. Tomography Analysis

We use 3-D azimuthal anisotropic inversion (Dunn et al., 2005) where the *V_p* model is parameterized with an isotropic component and two azimuthal anisotropy parameters. For each model grid, the anisotropic slowness, u_{ani} , is defined as

$$u_{ani} = \frac{u_{iso}}{1 + A\cos 2\theta + B\sin 2\theta}, \quad (1)$$

where u_{iso} is the isotropic slowness and θ is the raypath azimuth. The terms *A* and *B* are anisotropy parameters. The magnitude of anisotropy, *M*, is expressed as

$$M = 2\sqrt{(A^2 + B^2)}, \quad (2)$$

or the percentage of anisotropy, α ,

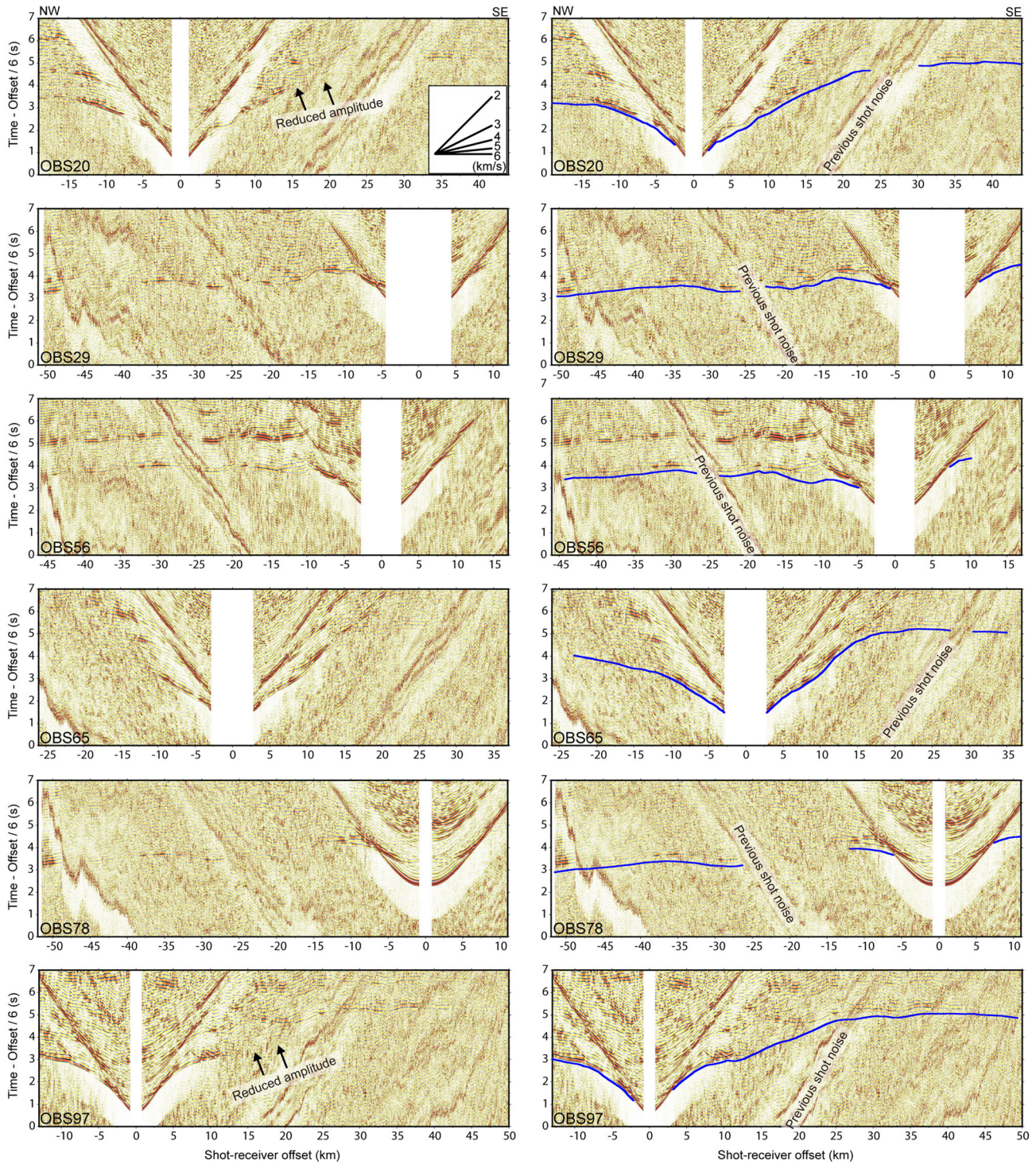


Figure 2. Examples of OBS record sections. Blue solid lines show picked arrival times. A 3- to 12-Hz band-pass filter and 3-s automatic gain control were applied. The reduction velocity is 6.0 km/s. Although strong water arrivals from previous shots overlap the primary refraction phases, first arrivals are clearly observed in the horizontal distance of 0–20, 25–45, and greater than 50 km.

$$\alpha = \frac{V_{fast} - V_{slow}}{V_{iso}} = \frac{M}{u_{iso} - \frac{M^2}{4u_{iso}}}$$

The fast direction, ψ , is

$$\psi = \frac{1}{2} \operatorname{atan} \left(\frac{B}{A} \right). \quad (3)$$

Theoretically, higher-order terms of even multiples of θ are also included in the formula (Backus, 1965). While previous studies show that 4θ variation is recognizable in traveltime data, it is difficult to constrain its spatial variation since it is roughly equivalent to or smaller than the traveltime pick uncertainty (Dunn, 2015). We also found a 4θ variation too small to model with our data, and we only examine the 2θ variation as described by the equation above.

We defined a model space of 70 km in the trench-normal direction (x axis), 16 km in the trench-parallel direction (y axis), and 18 km in the depth direction (z axis). The x axis in the trench-normal direction was oriented on seismic profile 05CM-04 (Barker et al., 2018). This model was discretized 0.2 km horizontally and 0.15 km vertically for forward calculation of traveltimes and raypaths. The upper surface of the model corresponds to the seafloor and was overlain by the water layer whose velocity was fixed at a constant value of 1.495 km/s.

Since the anisotropic velocity tomography is highly nonlinear and involves more parameters than isotropic analysis, the inverse calculation can be unstable even when a large quantity of data are available. To overcome this instability, we carefully constructed our starting model from existing, well-constrained velocity models and took multiple steps to sequentially develop toward anisotropic inversion. First, to obtain a stable starting model, a 2-D velocity model was created by taking the 1-D velocity profiles from two OBS refraction studies close to our study area, one from the forearc region and the other from the seaward side of the deformation front (Bassett et al., 2018; Kodaira et al., 2018) and linearly interpolating between them along the regional plate boundary model (Williams et al., 2013). The 2-D velocity model was then extended in the trench-parallel direction to create an initial 3-D model (Figure 3a). No anisotropy was assumed in the initial model. Despite this careful preparation, the initial model has large data misfits (the root-mean-squared, RMS, residual of 558 ms and normalized chi-square misfit of 242.72), which may end up in a local minimum after inversions especially for the anisotropic parameters. To stabilize the calculation, we took the average of the resultant V_p model after three iterations and the V_p values of the starting model (“first” initial model) to make a smooth “second” initial isotropic model (Figure 3b). We repeated this process two more times (resulting in “third” and “fourth” initial isotropic models; Figures 3c and 3d) until the changes in the V_p values became insignificant. Although the inversion for the initial model preparation is anisotropic, the V_p results are similar to those from an isotropic inversion since we assigned weaker damping for V_p and stronger damping for anisotropy in these inversions.

At each round of inversion steps, we employed different node spacing for the inverse problem. For the first round, 2–3 times larger spacing were used than those used for the final round to first solve for larger-scale velocity variations. The node spacings used in the final round for the isotropic slowness was 0.5 km in the x axis and 0.6 km in the y axis. Vertically, the node spacing was 0.5 km at 0- to 8-km depths, 1.0 km at 8- to 12-km depths, and 2.0 km from 12-km depth to the bottom of the model. The node spacing for anisotropic parameters were 1.5 km in the x and y axes and 0.5–2.0 km in the z axis. The inversion was regularized by smoothing and damping constraints that control the overall smoothness and stability of the final solution. In this tomography code, the user needs to assign the strength of horizontal and vertical smoothness and the damping term on the magnitude of model changes for both isotropic slowness and anisotropy. We determined the values of all these inversion parameters by referring to our past experiences using the same code (Dunn et al., 2017) and by assessing the results for different inversion parameter tests (see supporting information).

6. Results

6.1. V_p Structure

The final, preferred anisotropic model obtained after two iterations in the final round of inversion starting from the “fourth” initial model has the mean traveltime residual of 35 ms and the chi-square value of 0.86. Figures 4 and 5 show vertical cross sections and map view slices of the V_p values from this preferred model, respectively. One of the most important results is a low-velocity zone ($V_p = 1.6$ – 4.0 km/s)

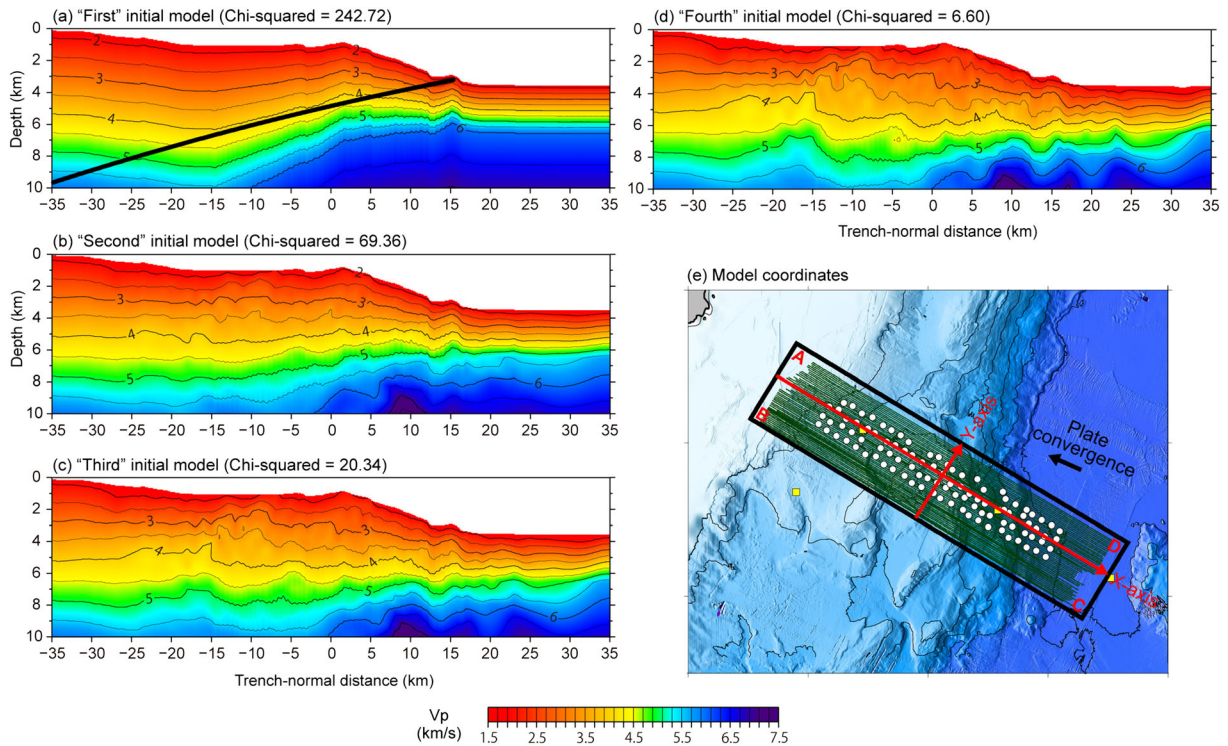


Figure 3. (a) Initial models used at different steps of the tomographic inversion. The vertical cross section for $y = 0$ km that coincides with the profile 05CM-04 is shown. The contour interval is 0.5 km/s. (a) The “first” initial model was created by taking velocity profiles from Bassett et al. (2018) and Kodaira et al. (2018) and smoothly connecting them by referring to the regional plate boundary model of Williams et al. (2013) (thick black curve). After three iterations of inversion using this initial model, we took the average of the resultant model and the initial model to make a smooth “second” initial model (b). This process was repeated two more times, resulting in “third” and “fourth” initial models (c and d), and then the final preferred model (Figures 4 and 5) was obtained after two iterations of inversion. (e) The inset map shows the model coordinate. A black arrow in the map indicates the convergence direction of the Pacific Plate relative to the North Island forearc at the Hikurangi Trough (Wallace et al., 2004).

observed at the frontal part of the upper plate (Figure 4). This zone forms an ~ 30 -km-wide and ~ 5 -km-thick accretionary wedge that is adjacent to a higher-velocity body ($V_p = 2.0$ – 4.5 km/s) on the landward side and corresponds to an area where multiple splay faults are developed (Barker et al., 2018; Figure 1d). By contrast, no active faults are imaged in the higher-velocity region marking the seaward edge of the north Tuaheni basin. In map view, the high-velocity body is oblique to the trench, rapidly narrowing the width of the accretionary wedge from ~ 30 km in the south to ~ 20 km at the northern end of the 3-D box (Figure 5).

Subducting along the Hikurangi Trough is the Hikurangi Plateau, a large igneous province of Cretaceous age with a crustal thickness over 10 km (Davy et al., 2008; Mochizuki et al., 2019). The structure of the incoming Hikurangi Plateau is different from typical oceanic crust and is characterized by thick low-velocity layers that shows a gradual increase in V_p with depth from ~ 1.6 km/s at the seafloor to ~ 5.0 km/s at 4-km depth below seafloor. This layer includes pelagic rocks of Paleogene to Miocene age and the Hikurangi basement mainly consisting of volcanoclastic rocks (Barnes et al., 2020). The lower volcanoclastic layer with V_p of 4.0–5.0 km/s extends in the downdip direction to beneath the accretionary wedge (Figure 4).

6.2. Anisotropy Structure

Figure 6a shows plots of traveltimes residuals calculated from the “first” initial model (Figure 3a), the final preferred model, and an isotropic model that was constructed in the same way as the preferred anisotropic model expect that only isotropic slowness parameters were inverted. This figure shows the best data fit for the preferred anisotropic model. Figure 6b indicates that many OBSs (those on the accretionary wedge and the north Tuaheni forearc basin in particular) exhibit clear variations in traveltimes residuals that can be approximated by a sine function of 2θ in the isotropic model (green ticks in Figure 6b). These traveltimes variations can be explained well by incorporating the anisotropic effect (red ticks in Figure 6b). The azimuthal variation in traveltimes residuals becomes smaller on the seaward side of the trench (Figure 6b).

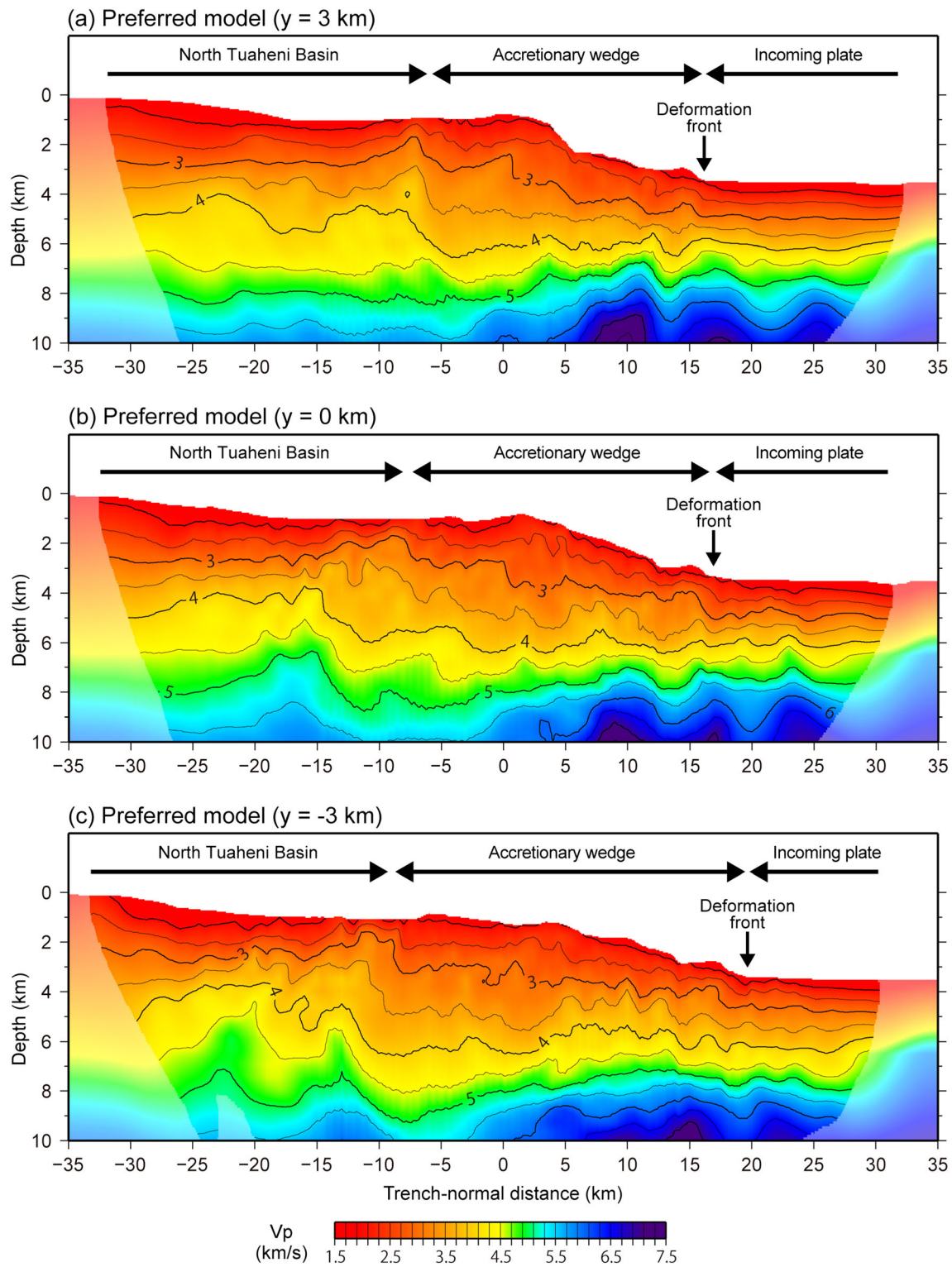


Figure 4. Vertical sections of V_p values from the preferred model. Three sections at $y = 3$ km (a), 0 km (b), and -3 km (c) are shown. The RMS traveltimes residual and normalized chi-square misfit of this model are 35 ms and 0.86, respectively. The contour interval is 0.5 km/s. Masked regions indicate areas with low resolution based on ray density and checkerboard tests. The coordinate system of the model (x and y axes) is shown in Figure 3.

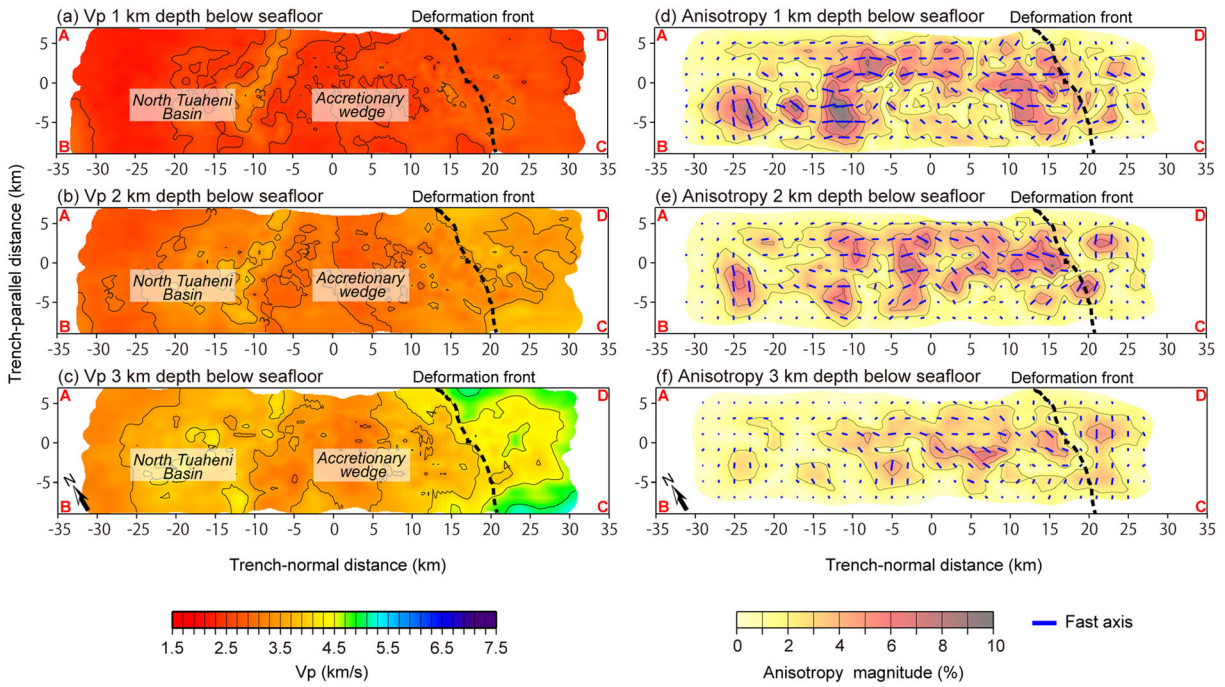


Figure 5. Subseafloor depth slices of V_p (a–c) and anisotropy magnitude (d–f) from the preferred model. The locations of these slices (rectangular box) and the coordinate system of the model (x and y axes) are shown in Figure 3. Black dashed line is the deformation front inferred from seafloor bathymetry. Blue ticks indicate the orientation of fast axes. Masked regions indicate areas with low resolution based on ray density and checkerboard tests (Figures S3 and S4).

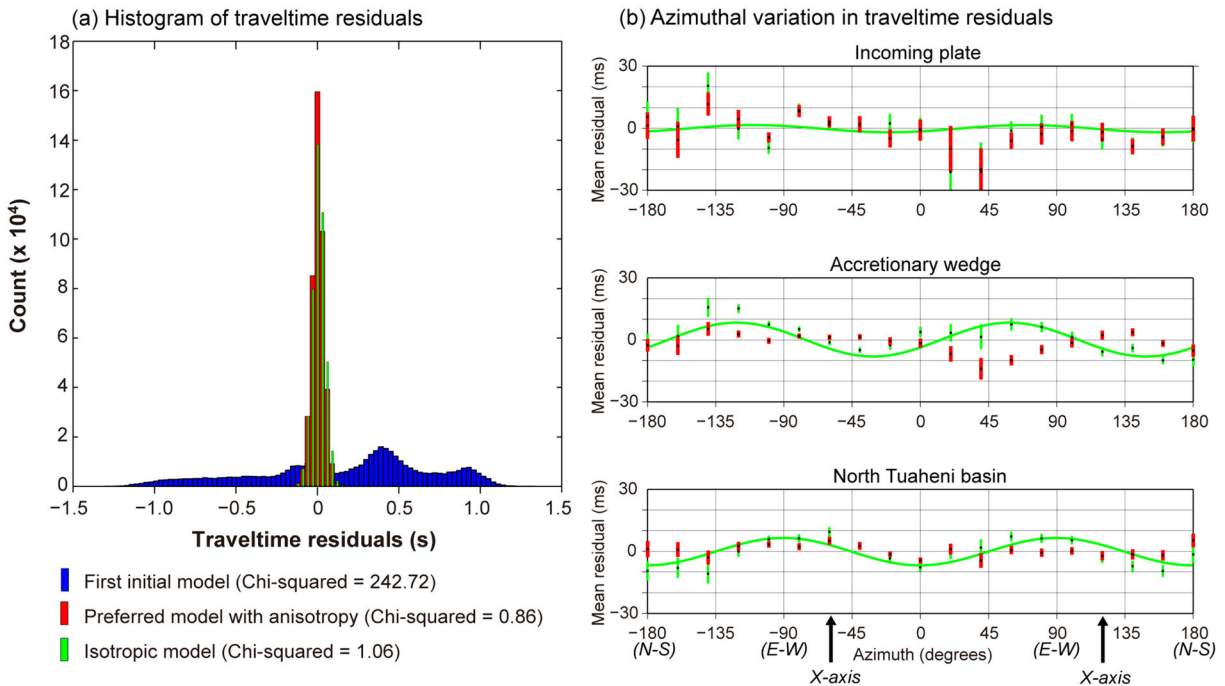


Figure 6. (a) Histograms of traveltimes residuals relative to the “first” initial model (blue), the final preferred model with anisotropy (red) and the isotropic model (green). (b) Mean traveltimes residual of the preferred anisotropic model (red bar) and the isotropic model (green bar) as a function of source–receiver azimuth. Shown here are the average values from OBSs on the incoming plate (indicated by white circles with a red circumference in Figure 1c), on the accretionary wedge (indicated by white circles with a purple circumference in Figure 1c) and on the north Tuaheni forearc basin (indicated by white circles with a blue circumference in Figure 1c). The mean residuals and standard deviations were calculated for azimuth bins of every 20° and using the rays whose maximum depths are less than 6 km. The shot–receiver azimuth is measured from north. The X axis is oriented to the southeast–northwest direction ($121^\circ/–59^\circ$) as indicated by black arrows. While the isotropic model shows clear variations in traveltimes residuals especially in the accretionary wedge and the forearc basin that can be expressed by a sine function of 2θ (green line), the preferred anisotropic model has better data fits independently of the azimuth direction.

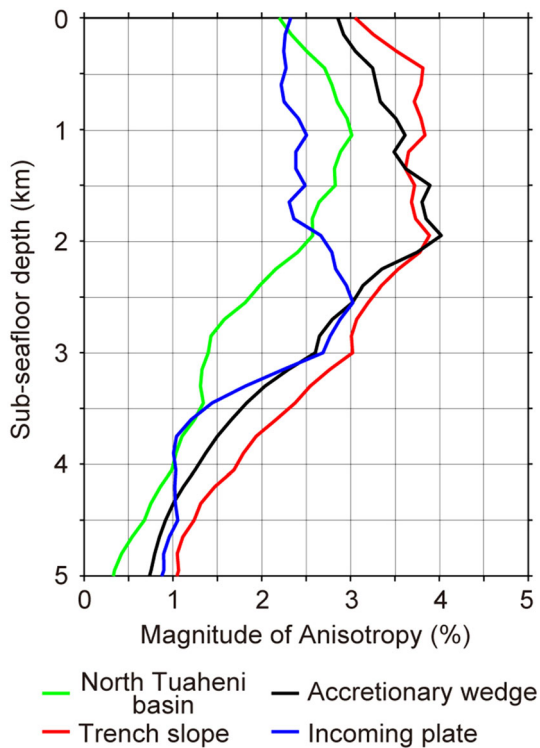


Figure 7. One-dimensional depth profiles of anisotropy magnitude from the preferred model. The colored curves show the mean values at each depth below the seafloor in the forearc basin (green; $x = -25$ to -15 km and $y = -4$ to 3 km), the accretionary wedge with flat seafloor (black; $x = -10$ to 0 km and $y = -4$ to 3 km), the trench slope (red; $x = 2$ to 15 km and $y = -4$ to 3 km), and the incoming plate (blue; $x = 19$ to 25 km and $y = -3.6$ to 3 km). The standard deviation of the 1-D profiles is about 1% for all locations.

Correspondingly, the 1-D depth profile of anisotropy shows that the accretionary wedge tends to show larger azimuthal anisotropy in the upper 2.0 km below the seafloor than the landward forearc basin and the seaward incoming plate (Figures 7 and S2). The map view slices reveal that areas with $>5\%$ anisotropy are found mostly in the accretionary wedge (Figure 5). This 5% value is the average over the scale length our model can resolve (2–4 km); we cannot exclude the possibility that a much higher magnitude of anisotropy than 5% exists along the faults beyond our resolution. The cross section shows that the anisotropic features are not ubiquitous and homogeneous within the overriding plate and tend to become larger in the vicinity of the fault locations (Figure 8).

The fast axes of V_p exhibit a clear spatial pattern: While they are mostly oriented in the trench-normal (i.e., plate convergence) direction in the accretionary wedge, they are rotated to the trench-parallel direction on the seaward side of the trench and in the landward north Tuaheni basin (Figures 5 and 9a). This regional variation is consistent with the results of shear wave splitting analysis (Zal et al., 2020; Figure 9b) and the regional stress field estimated by focal mechanism solutions (Townend et al., 2012). Occurrence of fast axes in the accretionary wedge agrees well with the directions of maximum horizontal stress inferred from borehole breakouts at Drilling Sites U1518 and U1519 (Figure 9a). These correlations demonstrate that our estimation of V_p anisotropy is consistent with other similar analyses and observations.

6.3. Model Resolution and Reliability

The reliability of obtained structural heterogeneities was evaluated by several different methods. Checkerboard tests using the same raypaths, matrix of partial derivatives, and smoothing/damping constraints as for the preferred model demonstrate that the anomaly pattern of 4 km horizontally and 3 km vertically is well recovered down to the depth of 6 km

below seafloor (Figure S3). Although slightly distorted and weaker at depths greater than 6 km, the checkerboard is recovered down to 9 km depth and we consider this to be the maximum depth of resolution in our velocity model. Smaller horizontal anomalies of 2 km are successfully reconstructed in the upper 4 km and partially recovered down to 6 km. These tests constrain the minimum size of velocity variations we can interpret. The checkerboard tests for anisotropy magnitude indicate that anisotropy is well resolved down to the depth of 4 km below seafloor and partially resolved down to 6 km beneath the accretionary wedge (Figure S4). Because anisotropy is calculated from rays of different azimuths, our maximum resolution depth is limited by the maximum offsets recorded in the margin-parallel direction.

The robustness of our velocity model was also examined by checking the dependency on the choice of inversion parameters (see Figures S5–S10). The alternative smoothing parameters for isotropic slowness yield models that have only small velocity differences with respect to the preferred model (<0.1 km/s in most parts of the model) (Figure S7). Different choices of smoothing parameters for anisotropy resulted in similar spatial pattern and magnitude in anisotropy (within 2% difference in most parts of the model), which strongly supports the validity of our anisotropy estimation (Figure S8). We also performed similar tests for the damping strength of V_p and anisotropy and confirmed that the range of acceptable solutions is relatively small (Figures S9 and S10).

Finally, we compared our V_p model with the detailed V_p structure obtained by the FWI analysis of the 05CM-04 reflection profile (Gray et al., 2019) and logging data at two drill sites within the 3-D box (Wallace et al., 2019) (Figure 10). Our velocity model has a spatial resolution of a few kilometers and thus is not sensitive to the abrupt velocity reductions in the upper ~ 200 m of the model that are suggested by the FWI analysis and logging data, which have their vertical resolution of $< \sim 100$ m. In addition, the

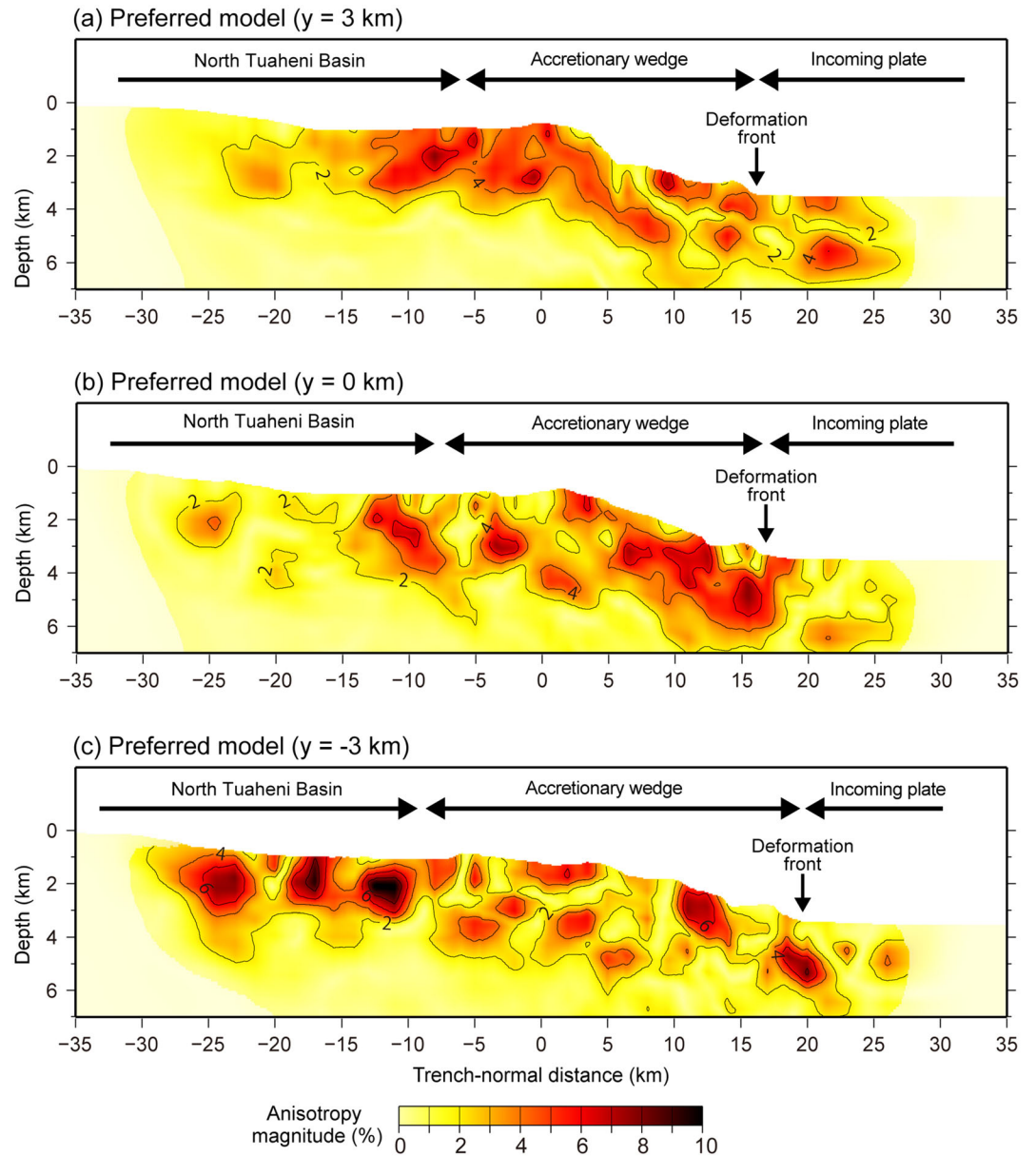


Figure 8. Vertical sections of anisotropy magnitude from the preferred model. Three sections at $y = 3$ km (a), 0 km (b), and -3 km (c) are shown. The contour interval is 2% . Masked regions indicate areas with low resolution based on ray density and checkerboard tests (Figures S3 and S4). The coordinate system of the model (x and y axes) is shown in Figure 3.

shallowest part of our velocity model may be poorly constrained due to the lack of very near-offset first arrivals. Otherwise, our V_p model generally shows difference less than 0.2 km/s from the FWI and logging data at depths greater than 200 m, suggesting that the velocity variations in our V_p model are real within the range of overlap and likely good approximations deeper within the section.

7. Discussion

7.1. Anisotropy Associated With Subduction Faults

Seismic anisotropy at shallow depths in subduction zones is an important indicator of the stress state and is commonly interpreted to be caused by preferentially oriented cracks in a compressional stress regime associated with plate subduction (Tonegawa et al., 2017; Zal et al., 2020). Our findings that (i) significant

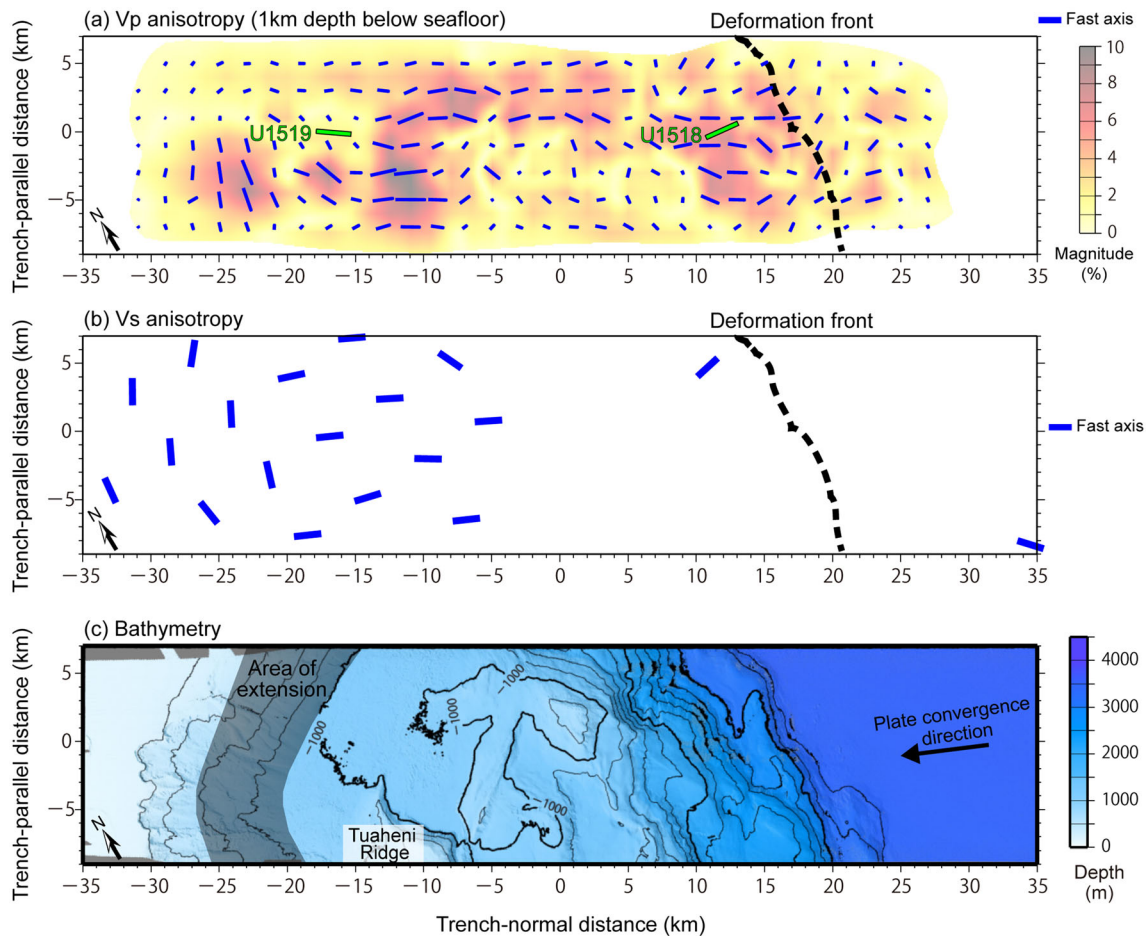


Figure 9. Map view slice of (a) anisotropy magnitude at 1-km depth below seafloor and comparison with (b) shear wave splitting anisotropy (Zal et al., 2020) and (c) seafloor depth. The fast axes of V_p agree well with the orientation of maximum horizontal stress (SH_{max}) inferred from borehole breakouts at Drilling Sites U1518 and U1519 (Wallace et al., 2019; green ticks) and shear wave anisotropy. At U1519, borehole breakouts with an approximate northeast-southwest ($054^\circ/234^\circ$) direction was observed between 600 and 650 m below seafloor (Wallace et al., 2019). At U1518, borehole breakouts have an azimuth of $173^\circ/353^\circ$ from which a SH_{max} orientation of east-is estimated. Blue ticks in (b) indicate the orientation of fast axes based on shear wave splitting (Zal et al., 2020). The seafloor bathymetry data in (c) was obtained during the 3-D seismic reflection cruise (Edwards et al., 2018). The study area includes the northern Tuaheni landslide complex (TLC north) and Tuaheni Ridge. A gray shade indicates the area of extension where normal faults across the upper slope of the north Tuaheni basin are distributed (Böttner et al., 2018). A black arrow in (c) shows the convergence direction at the Hikurangi trough between the Pacific Plate relative to the North Island forearc (Wallace et al., 2004).

anisotropy occurs associated with the active splay faults and the deformation front and (ii) the fast axes in the accretionary wedge lie parallel to the plate convergence direction suggest that the regional stress field and preferentially oriented cracks in the fault-bound blocks primarily control the seismic anisotropy. It is interesting that locations with large anisotropy tend to extend in the trench-parallel direction and some coincide with the steep slopes in seafloor bathymetry (Figure 9). Figure 7 compares the depth profile of anisotropy magnitude beneath the trench slope (that exhibits dip angles $>20^\circ$) with that below the accretionary wedge with flat seafloor and shows that the former has slightly larger anisotropy in the upper 1 km. This difference may reflect a gravitational effect pointed out by Araragi et al. (2015) that a gravitational stress caused by topographic slopes influences the principal stress direction and thus the seismic anisotropy at shallow depths. Our results indicate that this effect may also play a role in trench slopes in subduction zones.

The maximum magnitude of anisotropy we have observed ($>5\%$) is roughly equivalent to the values reported in oceanic spreading centers where the ridge-perpendicular tensile stress is dominant and thus likely to produce more cracks than at subduction zones (e.g., Dunn, 2015). The high-resolution velocity images produced by FWI revealed that some splay faults (but not all) were associated with low-velocity zones, suggesting that

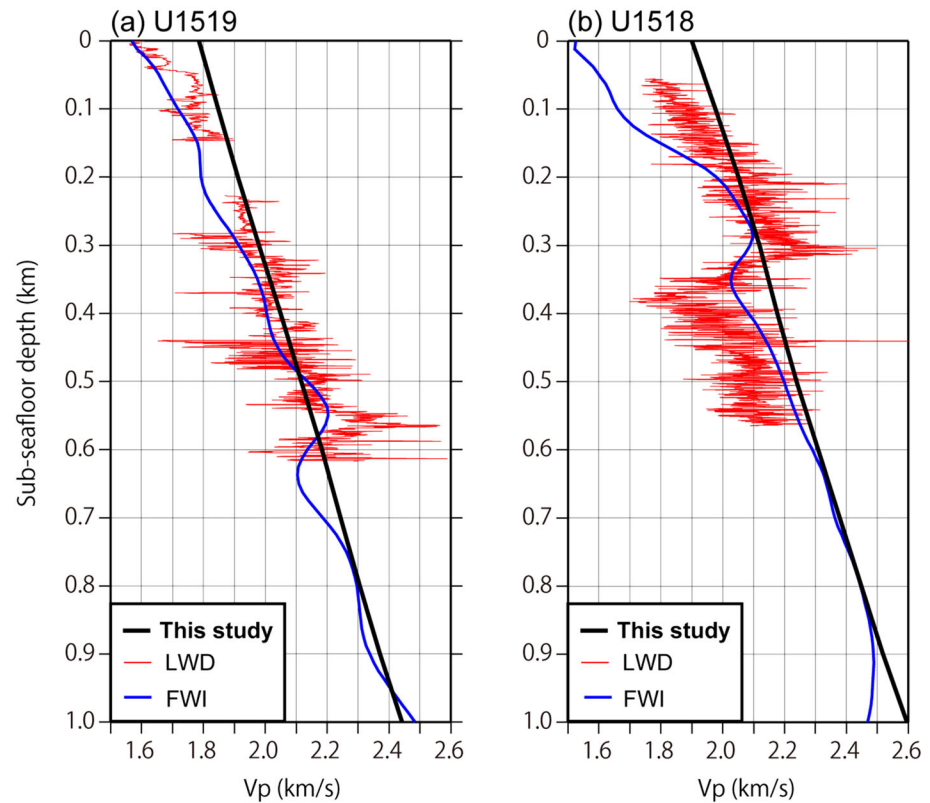


Figure 10. Comparison of our preferred velocity model with the logging-while-drilling (LWD) data (Wallace et al., 2019; red line) and the results from seismic full-waveform inversion analysis (FWI) (Gray et al., 2019; blue line) at drill sites of (a) U1519 and (b) U1518.

these faults may have high porosity and could act as fluid conduits (Gray et al., 2019). In the study area, it is expected from local seismicity that fluids released from the downgoing slab migrate into the overlying plate interface and upper plate (Shaddox & Schwartz, 2019; Todd et al., 2018; Warren-Smith et al., 2019). Such fluids contribute to increasing the crack density around the faults by keeping the cracks open at greater depths (e.g., Zatsepin & Crampin, 1997). However, not all splay faults are characterized by an across-fault velocity reduction and associated porosity increase. For example, while our V_p model indicates a high anisotropy area corresponding to the Pāpaku fault that is located in the trench slope (Figure 11), a low-velocity volume is not associated with this particular fault in the FWI analysis of Gray et al. (2019). In addition, core samples from U1518 that crosscut the Pāpaku fault at ~300-m depth suggest that there is not a significant increase in porosity at the fault zone (Fagereng et al., 2019). These considerations indicate that a factor other than preferentially oriented cracks may contribute to seismic anisotropy.

Although clay fabric is not observed in the core samples from the Pāpaku fault at U1518 (Fagereng et al., 2019), clay-rich sediments with evidence of ductile flow deformation are often observed at fault zones in subduction zones (Kinoshita et al., 2009; Tobin et al., 2001). In the northern Hikurangi margin, IODP drilling has confirmed that input sediments on the Hikurangi Plateau contain abundant clay minerals (Barnes et al., 2020). The sedimentary sequences are likely to stack and form coherent strata with a total thickness of up to several hundred meters in the vicinity of the fault zones during the process of accretion and/or subsequent deformation (Rowe et al., 2013). If the clay minerals in such thick sedimentary layers are preferentially aligned by the compressional stress by plate convergence, they may also result in significant upper plate anisotropy that can be detected by seismological methods.

7.2. Regional Stress Field Associated With Plate Subduction

Our velocity model revealed two other areas with different spatial orientation of anisotropy from the accretionary wedge which reflect variable stress field associated with plate subduction (Figure 5). First is the

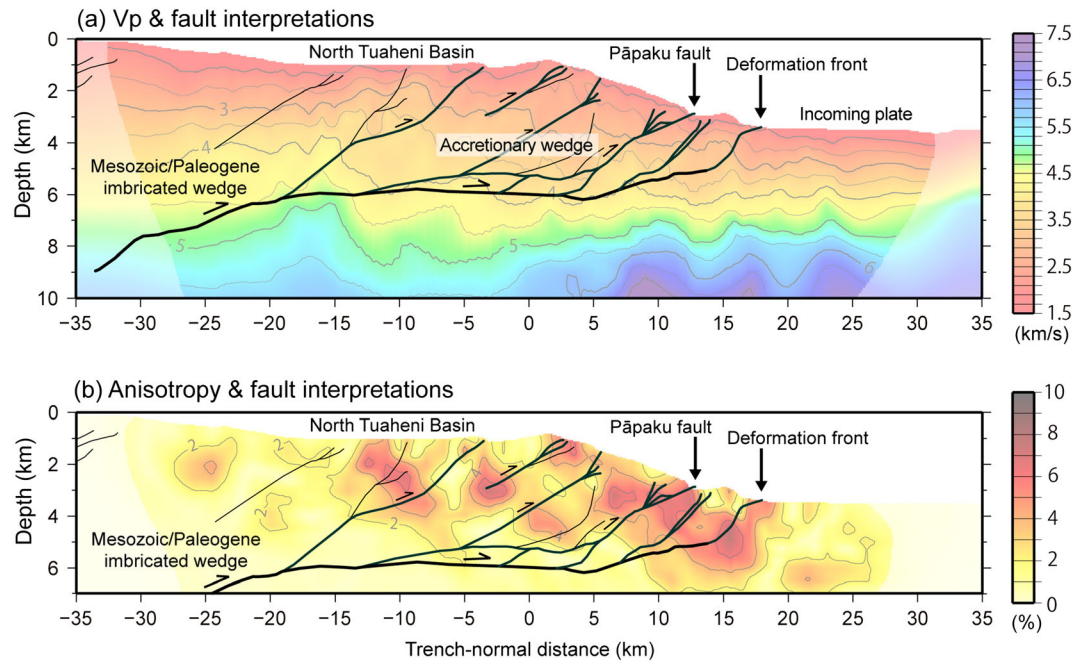


Figure 10. Comparison of (a) V_p and (b) anisotropy magnitude at $y = 0$ km from our preferred model with fault distribution (black lines) by Barker et al. (2018).

seaward side of the deformation front, where the fast axes of V_p are parallel to the strike of the trench at 2- to 3-km depths (Figures 5e and 5f). This feature is consistent with previous observation of anisotropy for the subducted Pacific Plate (Eberhart-Phillips & Reyners, 2009) and suggests that the maximum horizontal stress is oriented parallel to the trench. This stress regime is explained by the flexural bending of the incoming plate (e.g., Bodine et al., 1981). Although the overall magnitude is smaller (mostly less than 2%) compared to the magnitude of anisotropy in the accretionary wedge, this stress field may be active as implied by normal faults within the Hikurangi Plateau basement observed in seismic reflection data (Figure 1d). On the other hand, the fast axes at 1-km depth is more variable. The drill core data at U1520 suggests that this depth corresponds to the uppermost part of the Cretaceous volcanoclastic layer consisting of the Hikurangi Plateau (Barnes et al., 2020) and seismic studies suggest that its top surface exhibits significant relief with horizontal scales of <10 km (Barker et al., 2018; Barnes et al., 2020; Gray et al., 2019). We thus suggest that the scattered pattern of anisotropy in the shallowest part of the incoming plate may be a consequence of the stress field disturbed by structural heterogeneities at that depth.

The other area is the most landward part of the 3-D box where the fast axes of V_p rapidly change to the trench-parallel direction (Figures 5, 9, and 12). This change may be related to the Tuaheni Ridge and the edge of the North Tuaheni basin, in an area where forearc extension has been previously mapped (Böttner et al., 2018; Figures 9c and 12a). The variation in seismic anisotropy is consistent with the results of shear wave splitting analysis (Zal et al., 2020; Figure 9b). While the depth variation in anisotropy was not well constrained by Zal et al. (2020), our results demonstrate that the upper few kilometers in the overriding plate is the region which determines this spatial pattern.

It is also intriguing that the spatial variation in anisotropy correlates well with the structural heterogeneities within the overriding plate. Figure 12 shows that in the north Tuaheni forearc basin significant anisotropy exists just above two features consisting of high-velocity material with 4.0–5.0 km/s. These bodies are likely to be the lowest part of the overriding plate and probably associated with the Mesozoic and Paleogene imbricated wedge backstop. Forearc normal faulting has been identified in the Nankai accretionary margins and suggested to result from decoupling of shallow strata from the underlying compressional wedge (Gulick et al., 2010; Moore et al., 2013; Sacks et al., 2013). Böttner et al. (2018) were unable to identify the cause of extension, but we find that spatial orientation in anisotropy correlates well with the structural heterogeneities within the upper plate and supports the suggestion of local uplift giving rise to the extensional strain.

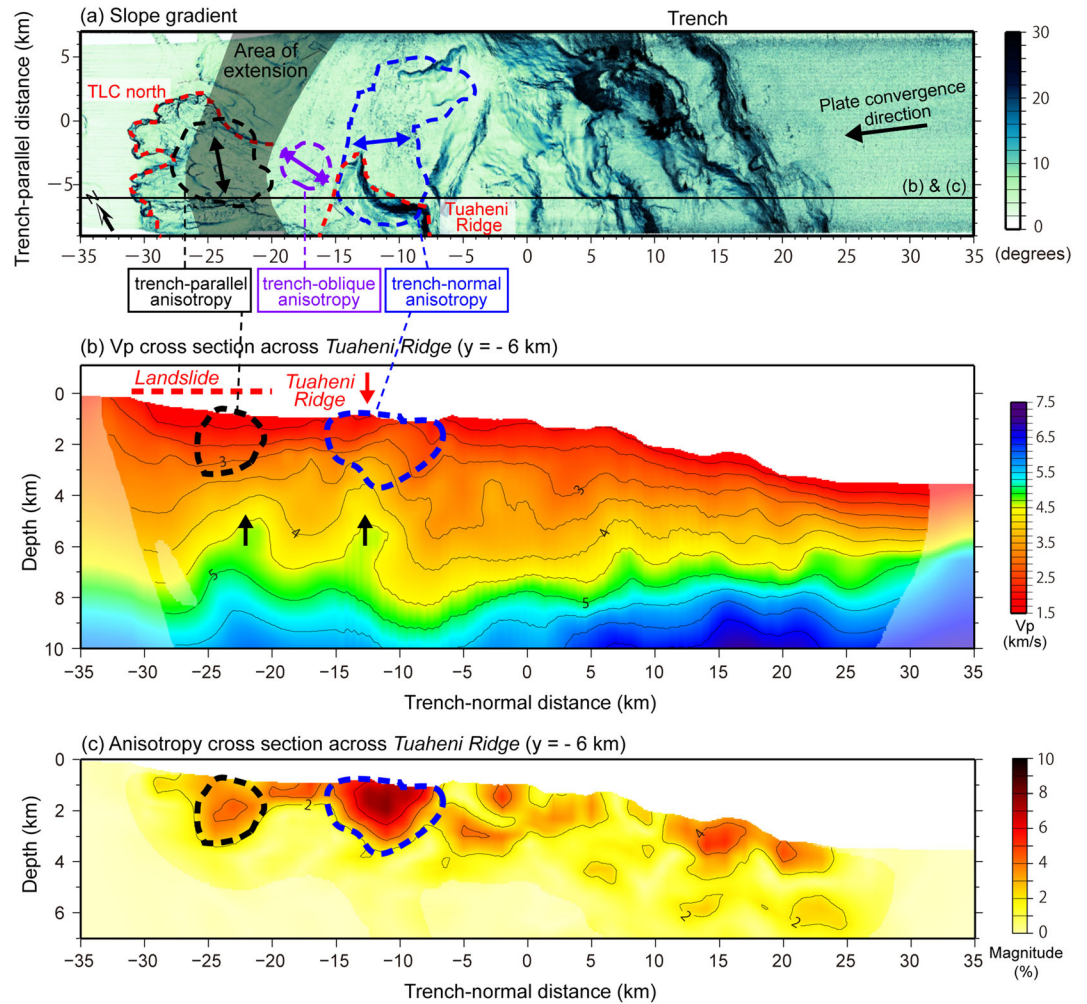


Figure 12. Spatial correlation of subsurface heterogeneities with the northern Tuaheni landslide complex (TLC north) and the Tuaheni Ridge. (a) Map of slope gradient highlighting the TLC north and the Tuaheni Ridge and (red dashed lines) where a rapid rotation of V_p fast directions occurs at shallow depths (as indicated by double-headed arrows). The location of trench-parallel anisotropy agrees well with the area of extension where normal faults across the upper slope of the north Tuaheni basin are distributed (Böttner et al., 2018; a gray shade). We calculated the slope gradient from the bathymetric grid data using GMT (Wessel & Smith, 1998). (b) The cross section of V_p at $y = -6$ km showing the deep high-velocity features just beneath the TLC north and the Tuaheni Ridge. (c) The cross section of V_p anisotropy at $y = -6$ km. Large anisotropy is observed beneath the TLC north and the Tuaheni Ridge (black and blue dashed lines).

7.3. Implications on Seamount Subduction

On the basis of the seismic reflection and magnetic data, it has been suggested that an ~20-km-wide seamount is subducting just beneath the central part of our 3-D survey area (Barker et al., 2018; Bell et al., 2010; Figure 1). The location and characteristics of the seamount are important because many previous studies have discussed seismic activity in relation to the seamount (e.g., Todd et al., 2018). In addition, a subducting seamount may have a strong control on seismogenic behavior, hydrological processes and the structural evolution of the plate interface and the overriding plate (Sun et al., 2020). At the proposed location of the seamount, our velocity model imaged a low-velocity ($V_p = 4.0$ – 5.0 km/s) volume and did not detect any rapid velocity increase with depth (Figure 11). This feature is consistent with the low seismic reflectivity at the top of the seamount while still accounting for the location of a high-relief magnetic source on the subducting plate (Barker et al., 2018).

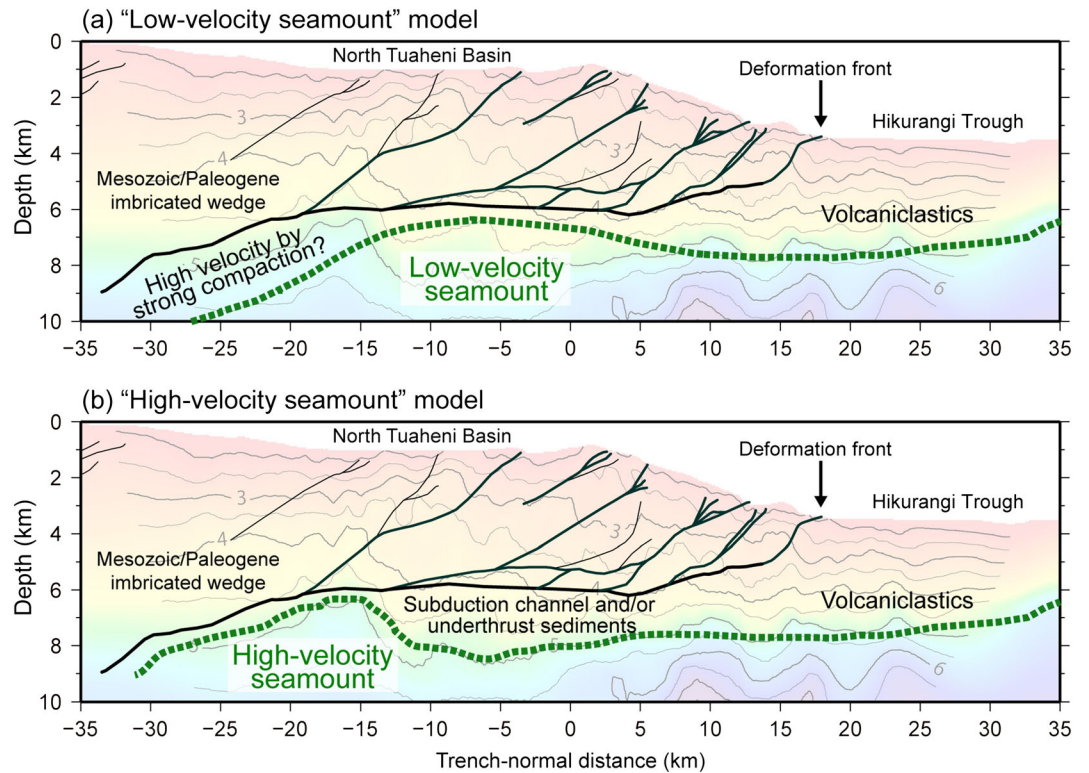


Figure 13. Two potential interpretations on subduction structure in the northern Hikurangi margin. (a) If the location of the subducting seamount by Barker et al. (2018) is correct, our V_p model suggests that the seamount exhibits low velocities which would imply the seamount is fractured. (b) Alternatively, the seamount is a high-velocity body, located further downdip.

Based on the currently available information, we propose two structural models focusing on the potential subducting seamount (Figure 13). First, if the location of the seamount by Barker et al. (2018) is correct, our V_p model suggests that the internal structure of the seamount may be heterogeneous containing substantial regions with low seismic velocities (Figure 13a). Although this explanation seems apparently counterintuitive, because seamounts are usually topographic manifestations of igneous intrusions and thus exhibit higher velocities than the surrounding areas, subducting seamounts may be able to exhibit lower velocities in the upper few kilometers due to significant fracturing and/or comprising extrusive volcanoclastic lithologies (Hammer et al., 1994). Indeed, low-velocity seamounts with a similar size are reported in the Ryukyu subduction zone, southwest Japan, where the Amami Plateau subducts beneath the Eurasian plate (Arai et al., 2017) and along the Kermadec arc where the Louisville Ridge intersects the Tonga-Kermadec subduction zone (Bassett & Watts, 2015).

The alternative model is that the seamount is a higher-velocity body, located ~10 km further downdip than previously thought (Figure 13b). This is the location where our velocity model shows high-velocity ($V_p > 5.0$ km/s) topography just below the plate interface. Correspondingly, the previous reflection studies revealed high-amplitude seismic reflectivity at the same place (Bell et al., 2010). The high reflectivity has been previously interpreted as low-velocity fluid-rich layers. Our velocity model may provide another interpretation for this reflectivity where top of the high-velocity seamount forms a thick reflective zone. This subduction model in Figure 13b suggests the seamount forms a low-velocity ($V_p = 4.0$ – 5.0 km/s) subducting channel in its wake that consists of sedimentary and volcanoclastic rocks in the process of subduction. However, this scenario would require a different interpretation of the magnetic data and the positive anomaly that is characteristic of nearby unsubducted seamounts (Barker et al., 2018). Future studies of subduction structure based on 3-D MCS reflection and OBS wide-angle reflection data, coupled with better constrained magnetic modeling, will provide more rigorous constraints of the subducting seamount.

8. Conclusions

We quantitatively constrained the 3-D V_p values and azimuthal anisotropy in the northern Hikurangi margin using seismic refraction data obtained by the NZ3D OBS experiment. We found evidence for fault-bound anisotropy and discovered that large anisotropy is associated with active thrust faults along the plate interface and within the upper plate. The localized pattern and anisotropy of >5% may suggest that not only preferentially oriented cracks but also fault-bound clay-rich sedimentary layers contribute to producing the significant upper plate anisotropy. The fast direction of the V_p is consistent with the plate convergence direction in the accretionary wedge and rotates to a trench-parallel direction beneath the Tuaheni basin and seaward incoming plate. We also found velocity variations associated with the subduction of the Hikurangi Plateau. We suggest that the subducting seamount, proposed by previous studies, shows low velocities due to fracturing and/or extrusive volcanoclastic rocks. Alternatively, it is possible the seamount is located ~10 km further downdip than previously thought.

Data Availability Statement

OBS data supporting the conclusions can be requested through JAMSTEC Seismic Survey Database (http://www.jamstec.go.jp/obsmcs_db/e/survey/data_area.html?cruise=TAN1803).

Acknowledgments

We thank the captains, crew, and onboard science parties of the R/V *Tangaroa* (TAN1712 and TAN1803) and the R/V *Marcus Langseth* (MGL18-01) for their dedicated contribution to the data acquisition during the cruises. We are also grateful to Robert Dunn for the permission for his tomographic code. Comments from M. Toriumi, T. Tonegawa, and K. Shiraishi were useful to interpret the anisotropy structure. Generic Mapping Tools (Wessel & Smith, 1998) was used to create figures. The data acquisition was financially supported by JAMSTEC, the NZ Ministry of Business Innovation and Employment (MBIE) Endeavour fund Hikurangi subduction earthquakes and slip behavior, Strategic Science Investment Fund (SSIF) to GNS Science, U.S. National Science Foundation (grant OCE15-59298), and Earthquake Research Institute, University of Tokyo. We also thank MBIE and the Tangaroa Reference Group for its support in granting sea time on R/V *Tangaroa* (TAN1712 and TAN1803). Constructive reviews by an anonymous referee, Audrey Galve, and the Associate Editor significantly improved the manuscript. R. A. was funded by the Japan Society for the Promotion of Science for Grant-in-Aid for Young Scientists (18K13641) and for Grant-in-Aid for Scientific Research on Innovative Areas (19H04629).

References

- Arai, R., Kodaira, S., Yamada, T., Takahashi, T., Miura, S., Kaneda, Y., et al. (2017). Subduction of thick oceanic plateau and high-angle normal-fault earthquakes intersecting the slab. *Geophysical Research Letters*, *44*, 6109–6115. <https://doi.org/10.1002/2017GL073789>
- Araragi, K. R., Savage, M. K., Ohminato, T., & Aoki, Y. (2015). Seismic anisotropy of the upper crust around Mount Fuji, Japan. *Journal of Geophysical Research: Solid Earth*, *120*, 2739–2751. <https://doi.org/10.1002/2014JB011554>
- Audoine, E., Savage, M. K., & Gledhill, K. (2004). Anisotropic structure under a back arc spreading region, the Taupo Volcanic Zone, New Zealand. *Journal of Geophysical Research*, *109*, B11305. <https://doi.org/10.1029/2003JB002932>
- Backus, G. E. (1965). Possible forms of seismic anisotropy of the uppermost mantle under oceans. *Journal of Geophysical Research*, *70*(14), 3429–3439. <https://doi.org/10.1029/JZ070i014p03429>
- Ballance, F. (1976). Evolution of the Upper Cenozoic magmatic arc and plate boundary in northern New Zealand. *Earth and Planetary Science Letters*, *28*(3), 356–370. [https://doi.org/10.1016/0012-821X\(76\)90197-7](https://doi.org/10.1016/0012-821X(76)90197-7)
- Barker, D. H. N., Henrys, S., Caratori Tontini, F., Barnes, P. M., Bassett, D., Todd, E., & Wallace, L. (2018). Geophysical constraints on the relationship between seamount subduction, slow slip, and tremor at the north Hikurangi subduction zone, New Zealand. *Geophysical Research Letters*, *45*, 23. <https://doi.org/10.1029/2018GL080259>
- Barker, D. H. N., Sutherland, R., Henrys, S., & Bannister, S. (2009). Geometry of the Hikurangi subduction thrust and upper plate, North Island, New Zealand. *Geochemistry, Geophysics, Geosystems*, *10*, Q02007. <https://doi.org/10.1029/2008GC002153>
- Barnes, P. M., Lamarche, G., Bialas, J., Henrys, S., Pecher, I., Netzeband, G. L., et al. (2010). Tectonic and geological framework for gas hydrates and cold seeps on the Hikurangi subduction margin, New Zealand. *Marine Geology*, *272*(1–4), 26–48. <https://doi.org/10.1016/j.margeo.2009.03.012>
- Barnes, P. M., Wallace, L. M., Saffer, D. M., Bell, R. E., Underwood, M. B., Fagereng, A., et al. (2020). Slow slip source characterized by lithological and geometric heterogeneity. *Science Advances*, *6*, eaay3314. <https://doi.org/10.1126/sciadv.aay3314>
- Bassett, D., Henrys, S. A., Barker, D. H. N., Arnulf, A. F., Arai, R., Kodaira, S., et al. (2018). The relationship between forearc structure and geodetic locking along the Hikurangi margin from SHIRE seismic data. *AGU Fall Meeting Abstract*, T53C-07.
- Bassett, D., & Watts, A. B. (2015). Gravity anomalies, crustal structure, and seismicity at subduction zones: 1. Seafloor roughness and subducting relief. *Geochemistry, Geophysics, Geosystems*, *16*, 1508–1540. <https://doi.org/10.1002/2014GC005684>
- Bell, R. Gray, M., Morgan, J., Warner, M., Fagereng, A., McNeill, L., et al. (2019). New Zealand 3D Full Waveform Inversion (NZ3D-FWI) 2017–2018 field acquisition report. *GNS Science report*, 2019/71, p. 79.
- Bell, R., Holden, C., Power, W., Wang, X., & Downes, G. (2014). Hikurangi margin tsunami earthquake generated by slow seismic rupture over a subducted seamount. *Earth and Planetary Science Letters*, *397*, 1–9. <https://doi.org/10.1016/j.epsl.2014.04.005>
- Bell, R., Sutherland, R., Barker, D. H. N., Henrys, S., Bannister, S., Wallace, L., & Beavan, J. (2010). Seismic reflection character of the Hikurangi subduction interface, New Zealand, in the region of repeated Gisborne slow slip events. *Geophysical Journal International*, *180*, 34–48. <https://doi.org/10.1111/j.1365-246X.2009.04401.x>
- Bird, P. (2003). An updated digital model of plate boundaries. *Geochemistry, Geophysics, Geosystems*, *4*(3), 1027. <https://doi.org/10.1029/2001GC000252>
- Bodine, J. H., Steckler, M. S., & Watts, A. B. (1981). Observations of flexure and the rheology of the oceanic lithosphere. *Journal of Geophysical Research*, *86*, 3695–3707. <https://doi.org/10.1029/Jb086ib05p0369>
- Böttner, C., Gross, F., Geersen, J., Crutchley, G. J., Mountjoy, J. J., & Krastel, S. (2018). Marine forearc extension in the Hikurangi margin: New insights from high-resolution 3-D seismic data. *Tectonics*, *37*, 1472–1491. <https://doi.org/10.1029/2017TC004906>
- Clark, K., Howarth, J., Litchfield, N., Cochran, U., Turnbull, J., Dowling, L., et al. (2019). Geological evidence for past large earthquakes and tsunamis along the Hikurangi subduction margin, New Zealand. *Marine Geology*, *412*, 139–172. <https://doi.org/10.1016/j.margeo.2019.03.004>
- Crampin, S. A. (1981). A review of wave motion in anisotropic and cracked elastic-media. *Wave Motion*, *3*(4), 343–391. [https://doi.org/10.1016/0165-2125\(81\)90026-3](https://doi.org/10.1016/0165-2125(81)90026-3)
- Davy, B., Hoernle, K., & Werner, R. (2008). Hikurangi Plateau: Crustal structure, rifted formation, and Gondwana subduction history. *Geochemistry, Geophysics, Geosystems*, *9*, Q07004. <https://doi.org/10.1029/2007GC001855>
- Doser, D., & Webb, T. H. (2003). Source parameters of large historical (1917 to 1961) earthquakes, North Island, New Zealand. *Geophysical Journal International*, *152*(3), 795–832. <https://doi.org/10.1046/j.1365-246X.2003.01895.x>

- Dunn, R. A. (2015). Tracking stress and hydrothermal activity along the Eastern Lau Spreading Center using seismic anisotropy. *Earth and Planetary Science Letters*, 410, 105–116. <https://doi.org/10.1016/j.epsl.2014.11.027>
- Dunn, R. A., Arai, R., Eason, D. E., Canales, J. P., & Sohn, R. A. (2017). Three-dimensional seismic structure of the mid-Atlantic ridge: An investigation of tectonic, magmatic, and hydrothermal processes in the rainbow area. *Journal of Geophysical Research: Solid Earth*, 122, 9580–9602. <https://doi.org/10.1002/2017JB015051>
- Dunn, R. A., Lekić, V., Detrick, R. S., & Toomey, D. R. (2005). Three-dimensional seismic structure of the Mid-Atlantic Ridge (35°N): Evidence for focused melt supply and lower crustal dike injection. *Journal of Geophysical Research*, 110, B09101. <https://doi.org/10.1029/2004JB003473>
- Eberhart-Phillips, D., & Reyners, M. (2009). Three-dimensional distribution of seismic anisotropy in the Hikurangi subduction zone beneath the central North Island, New Zealand. *Journal of Geophysical Research*, 114, B06301. <https://doi.org/10.1029/2008JB005947>
- Edwards, J., Bangs, N. L., Han, S., Barker, D. H. N., Harold, T., Reston, T. J., et al. (2018). High-resolution seafloor imaging of the diverse North Hikurangi Margin, including the creeping and catastrophic North Tuaheni Landslide. *AGU Fall Meeting Abstract*, T511-0311.
- Fagereng, Å., Savage, H. M., Morgan, J. K., Wang, M., Meneghini, F., Barnes, P. M., et al. (2019). Mixed deformation styles observed on a shallow subduction thrust, Hikurangi margin, New Zealand. *Geology*, 47, 872–876. <https://doi.org/10.1130/G46367.1>
- Gray, M., Bell, R. E., Morgan, J. V., Henrys, S., Barker, D. H. N., & the IODP Expedition 372 and 375 science parties (2019). Imaging the shallow subsurface structure of the north Hikurangi subduction zone, New Zealand, using 2-D full-waveform inversion. *Journal of Geophysical Research: Solid Earth*, 124, 9049–9074. <https://doi.org/10.1029/2019JB017793>
- Gulick, S. P., Bangs, N. L., Moore, G. F., Ashi, J., Martin, K. M., Sawyer, D. S., et al. (2010). Rapid forearc basin uplift and megasplay fault development from 3D seismic images of Nankai Margin off Kii Peninsula, Japan. *Earth and Planetary Science Letters*, 300(1–2), 55–62. <https://doi.org/10.1016/j.epsl.2010.09.034>
- Hammer, P. T. C., Dorman, L. M., Hildebrand, J. A., & Cornuelle, B. D. (1994). Jasper seamount structure: Seafloor seismic refraction tomography. *Journal of Geophysical Research*, 99(B4), 6731–6752. <https://doi.org/10.1029/93JB02170>
- Illsley-Kemp, F., Savage, M. K., Wilson, C. J. N., & Bannister, S. (2019). Mapping stress and structure from subducting slab to magmatic rift: Crustal seismic anisotropy of the North Island, New Zealand. *Geochemistry, Geophysics, Geosystems*, 20, 5038–5056. <https://doi.org/10.1029/2019GC008529>
- Kellett, R. L., Bassett, D., Arai, R., Obana, K., Stucker, V. K., Henrys, S. A., et al. (2018). TAN1712–1803 voyage report for ocean bottom seismograph recovery in support of seismic surveys (ORCSS 2 and 3): 3D survey offshore East Coast North Island. *GNS Science report*, 2018/36. <https://doi.org/10.21420/A8MV-S722>
- Kinoshita, M., Tobin, H., Ashi, J., Kimura, G., Lallemand, S., Scream, E. J., et al. (2009). NanTroSEIZE stage 1: Investigations of seismogenesis, Nankai Trough, Japan. In *Proceedings of the Integrated Ocean Drilling Program*, 314/315/316. College Station, TX: International Ocean Discovery Program.
- Kodaira, S., Fujie, G., Arai, R., Obana, K., Yamamoto, Y., Miura, S., et al. (2018). Along-strike variation of incoming plate to the Hikurangi seismogenic zone: Results from Seismogenesis at Hikurangi Integrated Research Experiment (SHIRE). *AGU Fall Meeting Abstract*, T511-0283.
- Lamb, S. H., & Bibby, H. M. (1989). The last 25 Ma of rotational deformation in part of the New Zealand plate-boundary zone. *Journal of Structural Geology*, 11(4), 473–492. [https://doi.org/10.1016/0191-8141\(89\)90024-2](https://doi.org/10.1016/0191-8141(89)90024-2)
- MGL1801 participants (2018). The NZ3D experiment—Adding a new dimension for understanding slow slip events. *GeoPRISMS Newsletter*, 40, 14–15.
- Mochizuki, K., Sutherland, R., Henrys, S., Bassett, D., Van Avendonk, H., Arai, R., et al. (2019). Recycling of depleted continental mantle by subduction and plumes at the Hikurangi Plateau large igneous province, southwestern Pacific Ocean. *Geology*, 47, 795–798. <https://doi.org/10.1130/G46250.1>
- Moore, G. F., Boston, B. B., Sacks, A. F., & Saffer, D. M. (2013). Analysis of normal fault populations in the Kumano Forearc Basin, Nankai Trough, Japan: 1. Multiple orientations and generations of faults from 3-D coherency mapping. *Geochemistry, Geophysics, Geosystems*, 14, 1989–2002. <https://doi.org/10.1002/ggge.20119>
- Okaya, D., Christensen, N., Stanley, D., & Stem, T. (1995). Crustal anisotropy in the vicinity of the Alpine Fault Zone. *New Zealand Journal of Geology and Geophysics*, 38(4), 579–583. <https://doi.org/10.1080/00288306.1995.9514686>
- Oshida, A., Kubota, R., Nishiyama, E., Ando, J., Kasahara, J., Nishizawa, A., & Kaneda, K. (2008). A new method for determining OBS positions for crustal structure studies, using airgun shots and precise bathymetric data. *Exploration Geophysics*, 39, 15–25. <https://doi.org/10.1071/EG08005>
- Pecher, I. A., Barnes, P. M., LeVay, L. J., & the Expedition 372A scientists (2019). Creeping gas hydrate slides. In *Proceedings of the International Ocean Discovery Program* (Vol. 372A). College Station, TX: International Ocean Discovery Program. <https://doi.org/10.14379/iodp.proc.372A.2019>
- Rait, G., Chanier, F., & Waters, D. (1991). Landward and seaward-directed thrusting accompanying the onset of subduction beneath New Zealand. *Geology*, 19(3), 230–233. [https://doi.org/10.1130/0091-7613\(1991\)019<0230:LASDTA>2.3.CO;2](https://doi.org/10.1130/0091-7613(1991)019<0230:LASDTA>2.3.CO;2)
- Rowe, C. D., Moore, J. C., Remitti, F., & the IODP Expedition 343/343T scientists (2013). The thickness of subduction plate boundary faults from the seafloor into the seismogenic zone. *Geology*, 41, 991–994. <https://doi.org/10.1130/G34556.1>
- Sacks, A., Saffer, D. M., & Fisher, D. (2013). Analysis of normal fault populations in the Kumano forearc basin, Nankai Trough, Japan: 2. Principal axes of stress and strain from inversion of fault orientations. *Geochemistry, Geophysics, Geosystems*, 14, 1973–1988. <https://doi.org/10.1002/ggge.20118>
- Shaddox, H. R., & Schwartz, S. Y. (2019). Subducted seamount diverts shallow slow slip to the forearc of the northern Hikurangi subduction zone, New Zealand. *Geology*, 47, 415–418. <https://doi.org/10.1130/G45810.1>
- Sun, T., Saffer, D., & Ellis, S. (2020). Mechanical and hydrological effects of seamount subduction on megathrust stress and slip. *Nature Geoscience*, 13, 249–255. <https://doi.org/10.1038/s41561-020-0542-0>
- Tobin, H., Vannucchi, P., & Meschede, M. (2001). Structure, inferred mechanical properties, and implications for fluid transport in the décollement zone, Costa Rica convergent margin. *Geology*, 29(10), 907–910. [https://doi.org/10.1130/0091-7613\(2001\)029<0907:SIMPAL>2.0.CO;2](https://doi.org/10.1130/0091-7613(2001)029<0907:SIMPAL>2.0.CO;2)
- Todd, E. K., Schwartz, S. Y., Mochizuki, K., Wallace, L. M., Sheehan, A. F., Webb, S., et al. (2018). Earthquakes and tremor linked to seamount subduction during shallow slow slip at the Hikurangi Margin, New Zealand. *Journal of Geophysical Research: Solid Earth*, 123, 6769–6783. <https://doi.org/10.1029/2018JB016136>
- Tonegawa, T., Obana, K., Yamamoto, Y., Kodaira, S., Wang, K., Riedel, M., et al. (2017). Fracture alignments in marine sediments off Vancouver Island from Ps splitting analysis. *Bulletin of the Seismological Society of America*, 107, 387–402. <https://doi.org/10.1785/0120160090>

- Townend, J., Sherburn, S., Arnold, R., Boese, C., & Woods, L. (2012). Three-dimensional variations in present-day tectonic stress along the Australia–Pacific plate boundary in New Zealand. *Earth and Planetary Science Letters*, 353–354, 47–59. <https://doi.org/10.1016/j.epsl.2012.08.003>
- Unglert, K. (2011). Crustal cracks in areas of active deformation: Correlation of GPS and seismic anisotropy. Master's thesis, Victoria University of Wellington, NZ.
- Wallace, L. M. (2020). Slow slip events in New Zealand. *Annual Review of Earth and Planetary Sciences*, 48, 175–203. <https://doi.org/10.1146/annurev-earth-071719-055104>
- Wallace, L. M., & Beavan, J. (2010). Diverse slow slip behavior at the Hikurangi subduction margin, New Zealand. *Journal of Geophysical Research*, 115(B12), B12402. <https://doi.org/10.1029/2010JB007717>
- Wallace, L. M., Beavan, J., McCaffrey, R., & Darby, D. (2004). Subduction zone coupling and tectonic block rotations in the North Island, New Zealand. *Journal of Geophysical Research*, 109, B12406. <https://doi.org/10.1029/2004JB003241>
- Wallace, L. M., Saffer, D. M., Barnes, P. M., Pecher, I. A., Petronotis, K. E., Levay, L. J., & the Expedition 372/375 Scientists (2019). Hikurangi subduction margin coring, logging, and observatories. In *Proceedings of the International Ocean Discovery Program* (Vol. 372-375). College Station, TX: International Ocean Discovery Program. <https://doi.org/10.14379/iodp.proc.372B375.2019>
- Wallace, L. M., Webb, S. C., Ito, Y., Mochizuki, K., Hino, R., Henrys, S. A., et al. (2016). Slow slip near the trench at the Hikurangi subduction zone, New Zealand. *Science*, 352, 701–704. <https://doi.org/10.1126/science.aaf2349>
- Wang, Z. (2002). Seismic anisotropy in sedimentary rocks, part 2: Laboratory data. *Geophysics*, 67(5), 1423–1440. <https://doi.org/10.1190/1.1512743>
- Warren-Smith, E., Fry, B., Wallace, L., Chon, E., Henrys, S., Sheehan, A., et al. (2019). Episodic stress and fluid pressure cycling in subducting oceanic crust during slow slip. *Nature Geoscience*, 12, 475–481. <https://doi.org/10.1038/s41561-019-0367-x>
- Webb, T. H., & Anderson, H. (1998). Focal mechanisms of large earthquakes in the North Island of New Zealand: Slip partitioning at an oblique active margin. *Geophysical Journal International*, 134(1), 40–86. <https://doi.org/10.1046/j.1365-246x.1998.00531.x>
- Wessel, P., & Smith, W. H. F. (1998). New improved version of the Generic Mapping Tools released. *Eos Transactions American Geophysical Union*, 79, 579. <https://doi.org/10.1029/98EO00426>
- Williams, C. A., Eberhart-Phillips, D., Bannister, S., Barker, D. H. N., Henrys, S., Reyners, M., & Sutherland, R. (2013). Revised interface geometry for the Hikurangi subduction zone, New Zealand. *Seismological Research Letters*, 84, 1066–1073. <https://doi.org/10.1785/0220130035>
- Wood, R., & Davy, B. (1994). The Hikurangi Plateau. *Marine Geology*, 118(1–2), 153–173. [https://doi.org/10.1016/0025-3227\(94\)90118-X](https://doi.org/10.1016/0025-3227(94)90118-X)
- Zal, H., Jacobs, K., Savage, M., Yarce, J., Mroczek, S., Graham, K., et al. (2020). Temporal and spatial variations in seismic anisotropy and V_p/V_s ratios in a region of slow slip. *Earth and Planetary Science Letters*, 532, 115970. <https://doi.org/10.1016/j.epsl.2019.115970>
- Zatsepin, S. V., & Crampin, S. (1997). Modelling the compliance of crustal rock-I. Response of shear-wave splitting to differential stress. *Geophysical Journal International*, 129(3), 477–494. <https://doi.org/10.1111/j.1365-246X.1997.tb04488.x>
- Zoback, M. L. (1992). First- and second-order patterns of stress in the lithosphere: The world stress map project. *Journal of Geophysical Research*, 97(B8), 11,703–11,728. <https://doi.org/10.1029/92JB00132>